INL/RPT-24-77346 Rev:000

Advancements in Multiphysics Microdepletion Analysis of an eVinci^{TM}-like Microreactor Leveraging OpenMC-CRAB Workflow

March 2024

Namjae Choi[1], Mustafa Jaradat[1], Vincent Laboure'[1], Jason Christensen[1], and Stefano Terlizzi[1]

[1]*Reactor Physics Methods and Analysis, Idaho National Laboratory*

INL is a U.S. Department of Energy National Laboratory
operated by Batelle Energy Alliance, LLC

INL/RPT-24-77346 Rev:000

Advancements in Multiphysics Microdepletion Analysis of an eVinci^{TM}-like Microreactor Leveraging OpenMC-CRAB Workflow

Namjae Choi[1], **Mustafa Jaradat**[1], **Vincent Laboure'**[1], **Jason Christensen**[1], **and Stefano Terlizzi**[1]

[1]**Reactor Physics Methods and Analysis, Idaho National Laboratory**

March 2024

Idaho National Laboratory
Nuclear Science and Technology
Idaho Falls, Idaho 83415

http://www.inl.gov

Prepared for the
U.S. Department of Energy
Office of Nuclear Energy
Under DOE Idaho Operations Office
Contract DE-AC07-05ID14517

Page intentionally left blank

SUMMARY

Nuclear microreactors (MRs) are a class of nuclear reactor technology, characterized by reduced dimensions, modular design, and reduced power output in contrast to conventional Light Water Reactors (LWRs). MRs are proposed for supplying electricity and eventual process heat to remote locations, such as military installations and disaster-affected areas. Current research work sponsored by the US Department of Energy Microreactor Program (MRP) is devoted to the development of novel modeling and simulation tools to better support MR vendors and regulatory bodies. Notably, the Nuclear Regulatory Commission (NRC) is projected to utilize the Comprehensive Reactor Analysis Bundle (CRAB) multiphysics software driver for executing both design and beyond-design-basis accident analyses. Furthermore, the NRC has been utilizing the MELCOR code to calculate mechanistic source terms during accidents. Since MELCOR relies on isotopic inventory and reactor temperature/power profiles under accident conditions, which theoretically can be derived from CRAB, the goal is to establish a comprehensive CRAB-MELCOR computational framework.

Past work was focused on testing and demonstrating CRAB's capability to generate results that can be used to inform mechanistic source term calculations in MELCOR. In particular, a computational workflow leveraging OpenMC-generated microscopic cross sections and CRAB was first applied to perform multiphysics microscopic depletion calculation followed by an accident scenario for a stylized microreactor problem. In fiscal year 2024, the research work has been focused on applying the OpenMC-CRAB workflow, which was first tested in fiscal year 2023, to a realistic 3D heat-pipe cooled MR problem representative of the eVinci^{TM} design. The latter computational problem was developed with inputs from Westinghouse Electric Company (WEC) to conserve selected neutronic and thermal characteristics of the eVinci^{TM} design without releasing proprietary data. The results of this simulation, encompassing isotopic inventory, power density distribution, and kinetic parameters, will inform both MELCOR and the WEC-developed FATE code for mechanistic source terms calculations. The results from the two codes will then be compared for code verification purposes.

This report contains the design characteristics of the realistic Heat Pipes-Cooled Microreactors (rHPMR) developed as a use-case for the verification exercise, and the current results for the multiphysics microscopic depletion performed with the OpenMC-CRAB workflow. The results include eigenvalue as a function of time, power distribution at EOL,in addition to nuclides inventory's time evolution and spatial distribution. Finally, we report improvements to the workflow efficiency achieved through a collaboration with the nuclear energy advanced modeling and simulation (NEAMS) programs. Through this collaborative effort, we were able to strongly decrease the computational time for the multiphysics microdepletion calculation (i.e., from 17.4 hours to 5.7 hours on 280 processors) in addition to simplifying the interface to generate isotopics spatial distribution utilizable by FATE and MELCOR. Future work, including the improvement of the current microscopic cross-sections' library and the simulation of an accident scenario at EOL, is also discussed.

ACKNOWLEDGEMENTS

The authors would like to acknowledge the contribution of Alexander Huning from Oak Ridge National Laboratory (ORNL), and James Scobel, Sung Jin Lee, and Patrick Kopfle from WEC for their feedback and insights on the rHPMR reactor. Specific contributions from the authors are detailed below:

1. Namjae Choi - Conceptualization, CRAB model development, Formal analysis, Writing, Investigation, Visualization.
2. Mustafa Jaradat - Conceptualization, OpenMC model development and cross sections generation, Formal analysis, Writing, Investigation, Visualization.
3. Vincent Labouré - Development of the rHPMR design.
4. Jason Christensen - Funding Acquisition.
5. Stefano Terlizzi - Conceptualization, Development of the rHPMR design, Serpent simulations, Formal analysis, Investigation, Writing, Review & editing, Visualization, Supervision.

This research made use of the resources provided by the US Department of Energy Microreactor Program (MRP) and the Nuclear Energy Advanced Modeling and Simulation (NEAMS) program managed by the Department of Energy's Office of Nuclear Energy, and of the resources of the High Performance Computing Center at Idaho National Laboratory, which is supported by the Office of Nuclear Energy of the U.S. Department of Energy and the Nuclear Science User Facilities under contract no. DE-AC07-05ID14517.

Page intentionally left blank

CONTENTS

FIGURES

TABLES

ACRONYMS

BOL	Beginning-of-life
CMFD	Coarse Mesh Finite Difference
CRAB	Comprehensive Reactor Analysis Bundle
EOL	End-of-life
HP	Heat Pipes
HPMR	Heat Pipes-Cooled Microreactors
INL	Idaho National Laboratory
LANL	Los Alamos National Laboratory
MOOSE	Multiphysics Object-Oriented Simulation Environment
MR	Microreactor
MRP	Microreactor Program
NEAMS	nuclear energy advanced modeling and simulation
NRC	Nuclear Regulatory Commission
rHPMR	realistic Heat Pipes-Cooled Microreactors
WEC	Westinghouse Electric Company

Page intentionally left blank

1. Introduction

The introduction of nuclear microreactors is expected to open up new markets for the nuclear power industry due to their inherent safety characteristics, small size, and potential to be cost-competitive in non-traditional market segments. Among the proposed MR designs, the monolithic Heat Pipes-Cooled Microreactors (HPMR) has emerged as one of the most promising options for remote application due to the characteristics of the heat pipes that allow to passively extract heat from the core. Heat pipes for nuclear applications are sealed stainless steel or FeCrAl tubes operating on the principle of phase-change by transporting heat from the in-core evaporator section to the ex-core condenser through isothermal vapor/liquid internal flow. No primary cooling loop, including large pipes and pumps, are needed, thus leading to the core design simplification and a minimum number of moving parts. The concept of HPMR was pioneered at Los Alamos National Laboratory (LANL) in the 1950s and it is currently pursued by several vendors in the United States, including WEC.

Current MRP-sponsored research work is devoted to the development of novel modeling and simulation tools to better support HPMR both vendors and regulatory bodies, including the NRC. Notably, the NRC is projected to utilize the CRAB multiphysics software driver for executing both design and beyond-design-basis accident analyses. Furthermore, the NRC has been utilizing the MELCOR code to calculate mechanistic source terms during accidents. Since MELCOR relies on isotopic inventory and reactor temperature/power profiles under accident conditions, which theoretically can be derived from CRAB, the goal is to establish a comprehensive CRAB-MELCOR computational framework. During fiscal year 2023, OpenMC-generated microscopic cross sections were used in CRAB for the first time to perform a multiphysics microdepletion analysis followed by a heat-pipe failure scenario for a stylized 2D HPMR [1]. The primary objective of the 2023 workscope was to test and demonstrate CRAB's capability to generate results that can be used to inform mechanistic source term calculations in MELCOR. In fiscal year 2024, the research has been focused on the application of the OpenMC-CRAB workflow, first demonstrated in fiscal year 2023, to analyze the rHPMR problem. This computational problem was developed with inputs from Westinghouse Electric Company (WEC) to conserve selected neutronic and thermal characteristics of the eVinci^{TM} design without releasing proprietary data. The results obtained

for the rHPMR problem, encompassing isotopic inventory, power density distribution, and kinetic parameters, will then be used to inform both MELCOR and the WEC-developed FATE code for mechanistic source terms calculations. Finally, the results from the mechanistic source terms calculations obtained from the two codes will be compared for code verification purposes.

This report contains the design specification of the realistic Heat Pipes-Cooled Microreactors (rHPMR) developed as a use-case problem for the verification exercise, and the current results for the multiphysics microscopic depletion performed with the OpenMC-CRAB workflow. The results include eigenvalue as a function of time, power distribution at EOL,in addition to nuclides inventory's time evolution and spatial distribution. Additionally, improvement to the workflow efficiency, achieved through a collaboration with the nuclear energy advanced modeling and simulation (NEAMS) programs, are here reported. Through this collaboration, we were able to strongly decrease the computational time for the multiphysics microdepletion calculation of a factor of 3.05 (i.e., from 17.4 hours to 5.7 hours on 280 processors) in addition to simplifying the interface to produce results utilizable by FATE and MELCOR. Future work, including the improvement of the current microscopic cross sections library and the simulation of an accident scenario at EOL are also discussed. The remainder of the report is structured as follows. The rHPMR design characteristics are reported in Section 2, while details on the CRAB model are presented in Section 3. Finally, analysis results are reported in Section 4, while conclusions and future work are addressed in Section 5.

2. The Realistic Heat Pipe cooled Microreactor

2.1 Problem Description

The rHPMR benchamark problem is a 5-MW_{th} heat-pipe cooled microreactor composed of 18 hexagonal assemblies arranged into two rings. The top and bottom surface of the 160-cm-high assemblies are surrounded by 20-cm-high axial beryllium reflectors. Each assembly contains 72 cylindrical fuel compacts and 19 HPs, drilled into a graphite monolith, with each HP surrounded by 6 fuel compacts to provide adequate cooling. Each fuel compact contains TRIstructural ISOtropic (TRISO) particles dispersed in a graphite matrix with a packing fraction of 36% and enrichment of 19.75%. TRISO particles have a UO_2 kernels and dimensions typical for fuel used

in the AGR-2 campaign [2].

The HPs are modeled as a mixture of SS-316 and sodium. A 0.05-cm gap is placed around HPs, fuel compacts, and the monolith to accommodate for thermal expansion and/or fission gas release. The core is surrounded by 12 control drums, with boron carbide employed as the absorbing material. Fig. 1 reports the radial and axial view of the rHPMRalong with a zoomed-in image of the fuel compacts. In Fig. 1, the yellow subdomains represent the heat pipes, the black circles are the fuel compacts, dark grey is used to identify the graphite monolith, light grey denotes the beryllium reflector, while green identifies the B_4C absorber. The reactor's geometrical specifications are reported in Tables 1, while Table 2 reports the material constituting each TRISO layer and the corresponding mass density. The rHPMR is envisioned to have a 4-years lifetime to reach a final fuel burnup of 21.76 MWd/kg that is in line with the value of 20.0 MWd/kg reported for the eVinci^{TM} reported in open literature [3].

Table 1: Geometrical specifications of the R-HPM. Linear dimensions in centimeters and angular dimensions in degrees.

Property	**Value**
Fuel Radius	1.0
TRISO packing fraction	36%
Fuel Compact Gap	0.05
Heat Pipe External Radius	1.1
Heat Pipe Gap	0.05
Pin Pitch	3.4
Assembly Pitch	32.0
Monolith Apothem	75.0
Gap around Monolith	0.05
Distance of Drums from Core Center	95.0
Poison Strip Internal Radius	14.0
Control Drum External Radius	15.0
Arc Width for Poison Strip	120.0
Gap around Control Drums	0.05
Reactor External Radius	112.0
Active Zone Height	160.0
Top Reflector Thickness	20.0
Bottom Reflector Thickness	20.0

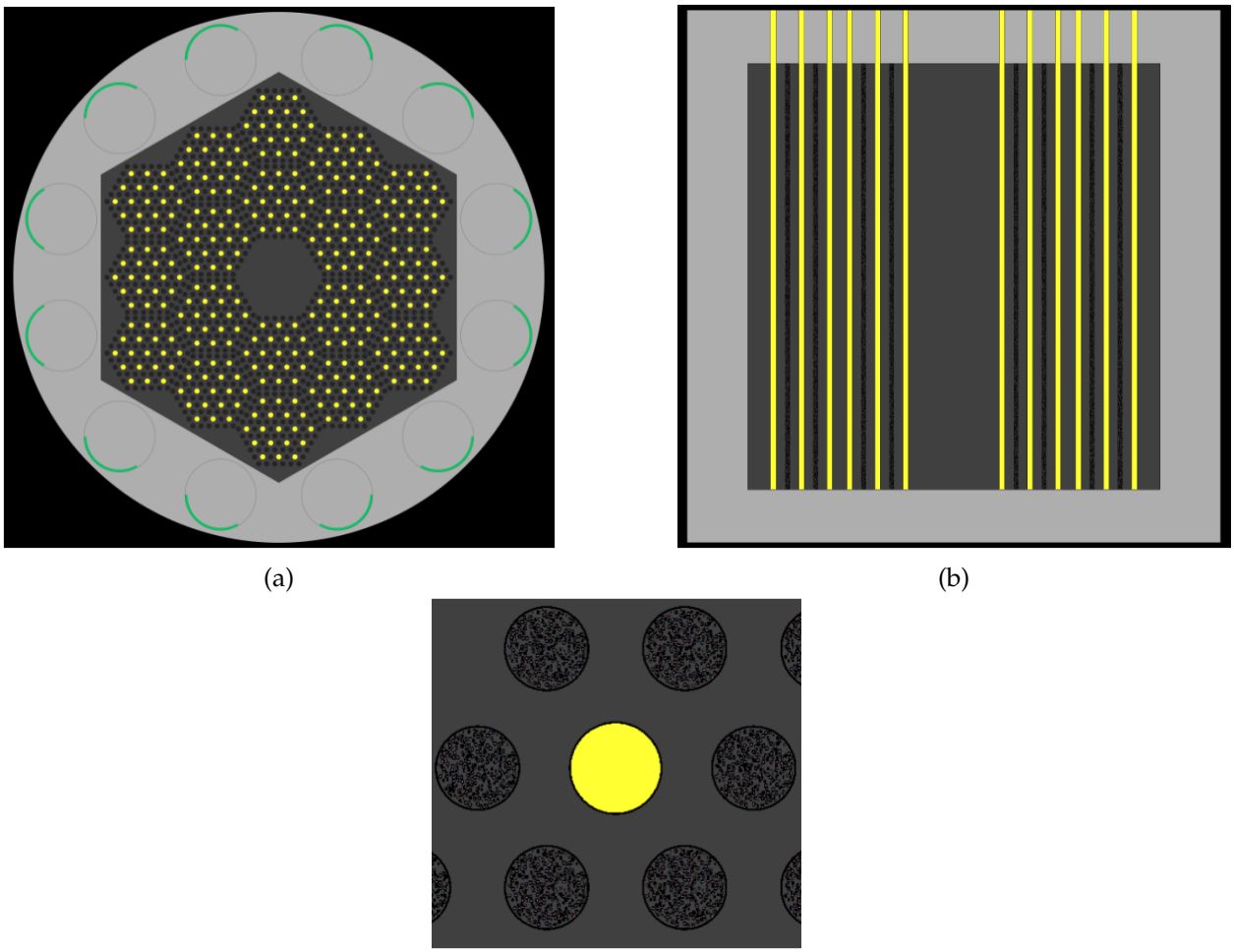

(a) (b)

(c)

Figure 1: Serpent-generated (a) radial view, (b) axial view, and (c) zoom-in for fuel compacts the rHPMR.

Table 2: Geometrical and material specifications for TRISO particles.

Component	Thickness μm	Material	Density g/cm^3
Kernel	250	UO_2	10.4
Buffer	100	Graphite	1.0
IPyC	40	Pyrolitic Carbon	1.9
SiC	35	SiC	3.2
OPyC	40	Pyrolitic Carbon	1.9

2.2 Neutronic Characterization

The neutronics studies contained in this section were conducted with Serpent (v. 2.2). Serpent was chosen for this scoping study due to its efficiency for problems characterized by a high num-

ber of surfaces [4, 5]. The simulations leveraged the ENDF/B-VIII.0 continuous energy library [6]. In Fig. 2.a, the fission rate and thermal flux distribution are plotted using hot and cold color schemes, respectively showing that the thermal flux peaks in the beryllium radial reflector and the central graphite block. The fission rate peaks at the periphery where the fuel faces reflecting materials. The reactor exhibits a thermal spectrum as shown by Fig. 2.b where the non-normalized spectrum per unit lethargy is shown.

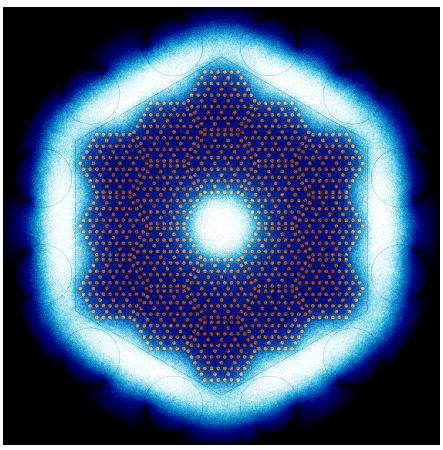

(a)

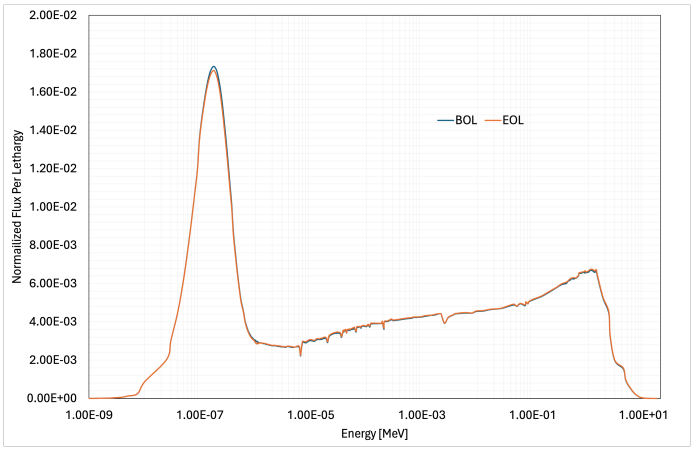

(b)

Figure 2: (a) Thermal flux and fission source rate spatial distribution in the mid-plane at BOL; (b) spectrum per unit lethargy at BOL and EOL.

The temperature reactivity feedback coefficients and kinetic parameters, which include the delayed neutron fraction and generation time, were calculated to characterize the reactor's behavior during transient and depletion scenarios. The fuel temperature reactivity coefficient and the isothermal temperature reactivity coefficient, denoted by α_{T_f} and α_{T_l}, respectively, are reported in Table 3 and computed with the following equation:

$$\alpha_{T_x} = \left(\frac{1}{k_{eff}(300)} - \frac{1}{k_{eff}(1100)} \right) \frac{10^5}{(800K)}, \tag{1}$$

where $k_{eff}(300)$ and $k_{eff}(1100)$ denote the value of the effective multiplication factor for the temperature of the material of interest at 300 K and 1100 K, respectively. The standard deviation is not reported because the analysis in this section primarily serves scoping purposes and is not utilized to verify the deterministic CRAB calculation provided in Section 4.3. Instead, the CRAB results are compared to those from OpenMC [7]. From Table 3, it is noticeable that the dominant

temperature feedback mechanism for the rHPMR is the fuel Doppler reactivity contribution, denoted by α_{Tf}, that ensures the controllability of the reactor. Additionally, the total control drums reactivity worth, denoted with α_θ, is computed to ensure the ability to bring the reactor to subcriticality at the EOL.

Table 3: Temperature reactivity feedback coefficient for the rHPMR at EOL.

Feedback Coefficient	Value
α_{T_f}, pcm/K	-4.59
α_{T_t}, pcm/K	-4.67
α_θ, pcm	13,174

The kinetic parameters are reported in Table 4 at both BOL and EOL. The results are obtained for hot conditions, that correspond to the reactor at an isothermal temperature of 1100 K.

Table 4: Kinetics parameters for the rHPMR

Kinetics Parameter	BOL	EOL
Λ (s)	1.95734E-04	2.08552E-04
β	6.63907E-03	6.10275E-03
β_1	2.90591E-04	2.52542E-04
β_2	1.12869E-03	9.12939E-04
β_3	1.16402E-03	1.11457E-03
β_4	2.69454E-03	2.46706E-03
β_5	9.20043E-04	1.00877E-03
β_6	4.41185E-04	3.46871E-04

The effective multiplication factor (k_{eff}) was ultimately calculated for the 4-year lifespan of the rHPMR. Fig. 3 illustrates the effective multiplication factor plotted against time, revealing that the reactor remains supercritical throughout its entire operational history. The results are obtained by depleting the fuel only with 100% nominal power (*i.e.*, 5 MW_{th}) and control drums are fully withdrawn. Additional simulations, not shown here, were performed to quantify the bias on k_{eff} when the TRISO particles are homogenization with the surrounding graphite matrix. It was found that the bias is approximately -2000 pcm for all the depletion steps, thus resulting in a constant vertical offset of the letdown curve shown in Fig. 3.

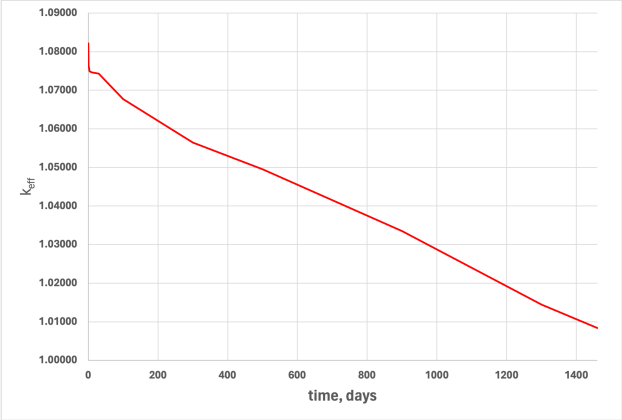

Figure 3: Effective multiplication factor vs. time for the rHPMR in hot conditions.

2.3 Thermal Margins Considerations

The analytical operational limits and the corresponding operational envelope for the heat pipes can be represented by a family of curves showing the maximum heat rate removable by the heat pipe vs. their representative operating temperature. This representative operating temperature is usually set to coincide with the saturation temperature of the vapor in the heat pipes for nominal operations [8]. The operational envelope is determined by the following limits [9]:

- The **capillarity limit** is related to the capillary pressure differences at the liquid-vapor interfaces in the evaporator and the condenser. In fact, if the capillary pressure is insufficient to push the liquid to flow from the condenser to the evaporator, hitting the capillarity limit will lead to a dryout of the evaporator wick.

- The **viscous limit** is connected to the balance between the total vapor pressure and the viscous forces in the vapor channel. If the heat pipes operate at low temperature, the vapor pressure in the evaporator may be very small, therefore leading to low mass flow rate of liquid from the condenser to the evaporator.

- The **sonic limit** is typically experienced in liquid metal heat pipes at the startup or in low-temperature conditions, therefore resulting in choked, or sonic, vapor flow.

- The **entrainment limit** derives from the interaction between the countercurrent liquid and vapor flows and the consequent viscous shear forces occurring at the liquid–vapor interface, which can inhibit liquid return to the evaporator.

- The **boiling limit** is related to the generation of nucleate boiling in the wick structure due to high heat fluxes. This phenomenon may lead to vapor being trapped in the wick, thus blocking liquid return and resulting in evaporator dryout.

The curves corresponding to these five limits can be generated with Sockeye [10]. The latter is a MOOSE-based heat-pipe analysis tool contained in CRAB whose primary purpose is to provide a transient heat pipe simulation tool analysis capability for nuclear microreactors. The Sockeye-generated operational limits for a 1.1-cm radius HP are shown in Fig. 4. The area under the curves depicted in Fig. 4 can be interpreted as the operating space for this heat pipe. It is noticeable that the maximum heat rate removable by a single heat pipes for 1100 K is 20 kW that is in excess of the 15 kW that is the average flux to be extracted per heat pipe in nominal conditions, thus showing the feasibility of the rHPMR design.

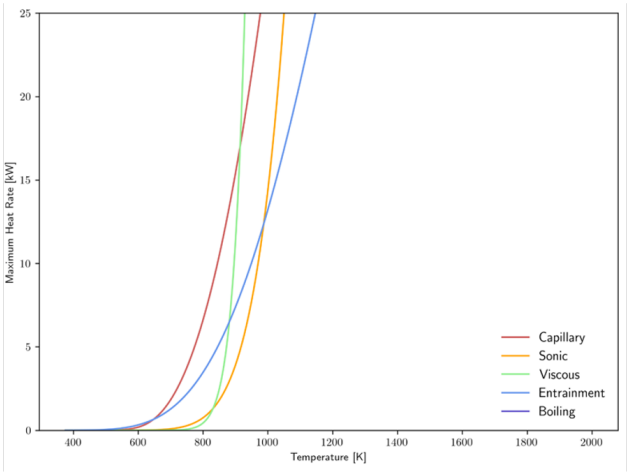

Figure 4: Analytical operational limits for 1.1-cm radius heat pipes in operation conditions for rHPMR

3. Codes and Computational Workflow

Figure 5 illustrates the computational workflow employed for conducting the multiphysics microdepletion analysis. For a comprehensive description of CRAB and its constituent codes, Griffin, Bison, and Sockeye, please refer to Refs. [1, 10–12] for detailed descriptions. A detailed explanation of the numerical scheme follows below.

1. **Preliminary operations**. The preliminary operations include:

- Mesh generation: mesh exodus files for the full-reactor geometries are generated using the MOOSE reactor module [13]. The exodus files containing the meshes for each single-physics solver is then used as input in Griffin and Bison. Details on the generated meshes can be found in Section 4.1.
- Microscopic cross sections generation. Microscopic cross sections are generated and pre-tabulated for the full-core as a function of local temperature using the OpenMC Monte Carlo code. [7]. The OpenMC-generated microscopic cross sections are then imported into Griffin through an OpenMC cross sections converter developed for this work [1].

2. **Multiphysics Depletion Calculations**. For each time depletion step:

   (a) **Eigenvalue Multiphysics Calculation**. Griffin and Bison are used to perform the depletion analysis. As noticeable from Fig. 5, for each time step, Griffin is used to solve the eigenvalue transport equation from which the power density spatial distribution, denoted as $P_d(\vec{x})$, is computed. The power density is then passed to the Bison full core heat transfer input where it is used as source term for the heat transfer equation. The solid temperature calculated by Bison, denoted as $T(\vec{x})$ in the figure, is then passed back to Griffin where is it utilized to update the value of the microscopic cross sections. The Picard iteration between Griffin and Bison is repeated until the neutron flux residual is below a pre-set tolerance.

   (b) **Depletion**. The angle- and energy-integrated neutron fluxes, denoted as $\phi(\vec{x})$, calculated within the eigenvalue multiphysics calculation, is then used within the CRAM solver in Griffin to evolve the isotopic inventory for a single time step, thus obtaining a new set of nuclides spatial distribution, denoted as $N_i(\vec{x})$ in Fig 5.

4. Numerical Results

This section reports the numerical results for the rHPMR model using the OpenMC-CRAB workflow. Sections 4.1–4.2 describe the mesh generation procedure and the cross-section generation strategy, respectively. The verification of the neutronic solver is then reported in Section 4.3,

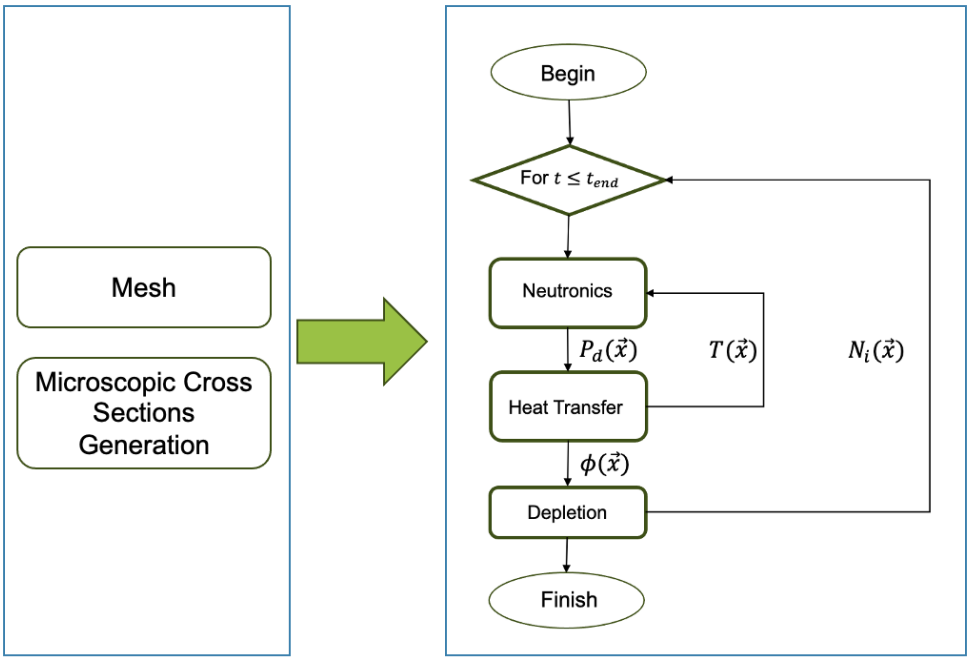

Figure 5: Flowchart for the microdepletion multiphysics calculation.

while the coupled multiphysics solution at BOL is reported in Section 4.4. Finally, the results for the multiphysics depletion analysis are reported in Section 4.5.

4.1 Mesh Generation

Two meshes were prepared for the multiphysics computations performed in this section. Fig. 6 reports the mesh for the neutronic transport calculation in Griffin. As noticeable, for the rHPMR problem, a one-twelfth radially reflected geometry was built by exploiting the problem's symmetry to minimize the number of degrees of freedom. The latter contains 196,900 elements distributed on 20 extruded layers. The mesh was generated using the reactor module in MOOSE. This module aims to improve the MOOSE-based workflow by allowing users to build common geometries encountered in nuclear reactor neutronic and heat transfer analyses conducted within the MOOSE framework [13]. The Bison mesh is obtained from the neutronic mesh in Fig. 6 by removing the gaps and the heat pipes subdomains and is therefore not shown in the figure.

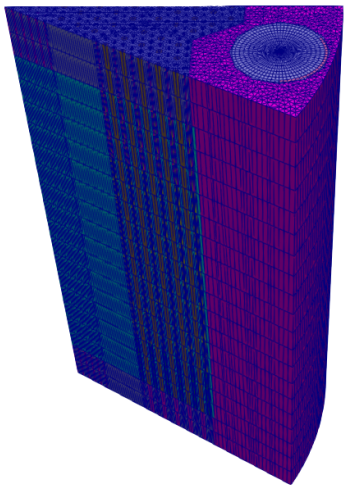

Figure 6: Neutronic mesh on which the multigroup neutron transport equation is solved.

4.2 Cross Sections Generation

OpenMC was used to generate multigroup microscopic cross sections for the Griffin deterministic neutron transport calculations. OpenMC was chosen over other MC codes (e.g., Serpent) for its ability to easily generate multigroup microscopic cross sections including the group-to-group scattering cross sections that cannot be generated in Serpent. The full-core model created in OpenMC for generating microscopic cross sections in multigroup format is depicted in Figure 7. These cross sections are computed using an 11-energy group structure, as detailed in Table 5. The selection of this 11-group energy structure was influenced by its prior utilization in various microreactors, including the SiMBA problem and the Empire reactor [14]. The microscopic cross sections are tabulated with respect to the local value of the temperature for 294 isotopes within the fuel. These isotopes include pseudo-isotopes defined to conserve the decay heat. The tabulation with respect to the temperature is performed by increasing the temperature uniformly for the whole reactor in increment of 100 K from 700 K to 1400 K that are considered the operation envelope for the reactor. Future enhancements will concentrate on refining the tabulation by incorporating burnup as an additional parameter. In this calculation, only the fuel undergoes depletion (control drums are excluded) and the TRISO particles are homogenized by volume with the graphite in the fuel compacts to save on computational time. Future iterations on the cross sections library will focus on the explicit inclusion of the TRISO particles in the cross sections gen-

erating file. The cross sections generated by OpenMC are converted into Griffin-readable ISOXML format using a newly developed OpenMC-to-ISOXML converter, which was partially developed for this project.

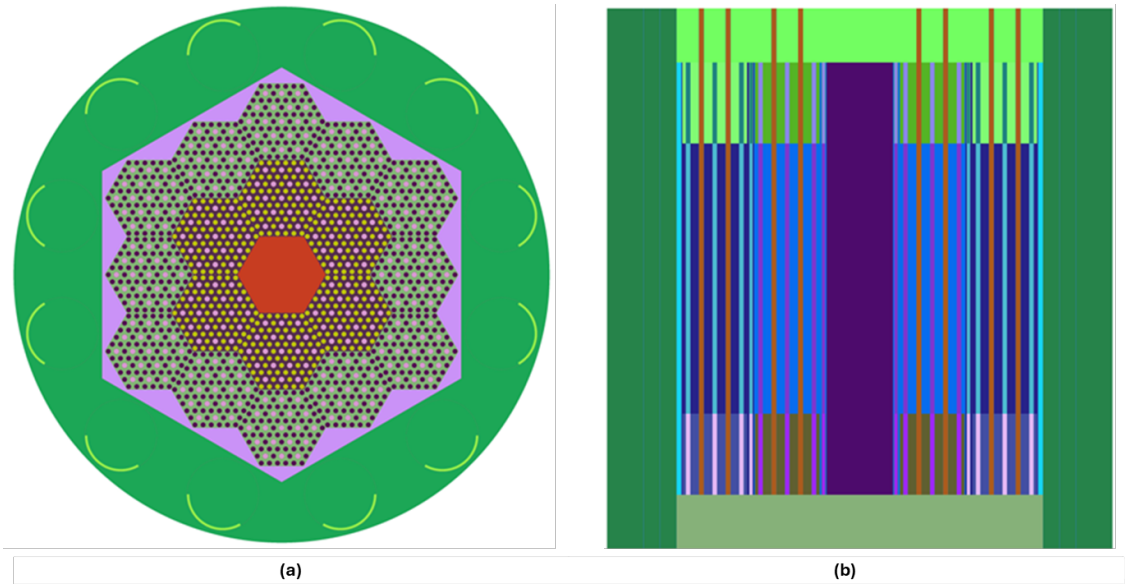

Figure 7: OpenMC model for cross sections generation.

Table 5: Neutron energy group boundaries for the 11 group structure.

Group	Upper Energy [eV]	Lower Energy [eV]
1	4.000E+07	8.210E+05
2	8.210E+05	1.830E+05
3	1.830E+05	4.900E+04
4	4.900E+04	4.540E+02
5	4.540E+02	4.810E+01
6	4.810E+01	9.880E+00
7	9.880E+00	4.000E+00
8	4.000E+00	1.000E+00
9	1.000E+00	3.200E-01
10	3.200E-01	6.700E-02
11	6.700E-02	1.000E-05

4.3 Neutronics Model Verification

To verify the consistency of the OpenMC and Griffin models, neutronics-only calculations were executed at various temperature points, and the Griffin-computed effective multiplication factor was compared against the one generated within the reference OpenMC calculation. The Griffin

calculations were conducted utilizing 6 azimuthal angles and 3 polar angles in octant (totaling 144 directions) and P_3 anisotropic scattering to account for the anisotropic scattering reaction resulting from the interaction of neutrons with the beryllium reflector. With these parameters, each simulation required approximately 22 to 24 minutes to converge on 48 processors.

Table 6 reports the effective multiplication factor computed by Griffin and OpenMC for each state point. The effective multiplication factor difference between Griffin and OpenMC is 382 pcm on average with random deviations depending on the temperature. There is no noticeable trend in the error depending on the temperature; namely, the temperature coefficients are consistent. Considering that beryllium has high degree of scattering anisotropy and that Monte Carlo method cannot rigorously tally high-order scattering matrices, the errors are considered acceptable [15].

Table 6: Comparison of Griffin eigenvalues against reference OpenMC eigenvalues at different temperatures. Standard deviations and differences are in pcm.

Temperature (K)	**OpenMC (std.)**	**Griffin**	**Diff.**
700	1.07745 (15)	1.08158	413
800	1.07184 (14)	1.07563	379
900	1.06553 (14)	1.06943	390
1000	1.06038 (15)	1.06421	383
1100	1.05522 (14)	1.05892	370
1200	1.04983 (14)	1.05338	355
1300	1.04550 (14)	1.04925	375
1400	1.04128 (14)	1.04520	392

4.4 Multiphysics Analysis at BOL

A steady-state multiphysics calculation was performed by coupling Griffin and Bison to obtain the coupled neutron flux and temperature distributions at BOL. Currently, the heat pipes are considered as a heat sink via a convective boundary condition within the heat transfer model. This boundary condition utilizes a secondary fluid temperature of 800K as T_∞ and an effective heat transfer coefficient computed from a Sockeye heat-pipe-only calculation. In forthcoming computations, this simplistic approach will be superseded by explicit modeling of heat pipes using Sockeye.

The coupled steady-state calculation was executed on a single node of the INL Sawtooth cluster (equivalent to 48 processors), totaling 31 minutes of computing time. The effective multipli-

cation factor obtained from the coupled calculation is 1.05114, which lies between the 1200K and 1300K cases in the standalone neutronics results outlined in Table 6. This falls within an expected range when considering the steady-state temperature distributions depicted in Fig. 8 for the axial and radial mid-plane. Notably, the maximum and minimum temperatures of the fuel are observed to be 1288 K and 1016 K, respectively. The temperature distribution unveils abrupt changes on the sides of several interfaces: 1) between fuel rods and monolith, 2) between heat pipes and monolith, 3) between monolith and reflector, and 4) between control drum and reflector. These discontinuities arise from the presence of air-filled gaps, indicating the accurate modeling of thermal contact between the monolith and other reactor components. Fig. 9 and Fig. 10 demonstrate the fast (group 1), intermediate (group 6), and thermal (group 11) flux distributions of the axial and radial mid-planes. The effect of temperature discontinuity due to the presence of the gaps together with the effect of the thermal neutrons' absorption is noticeable by observing the thermal flux distribution in the drum region.

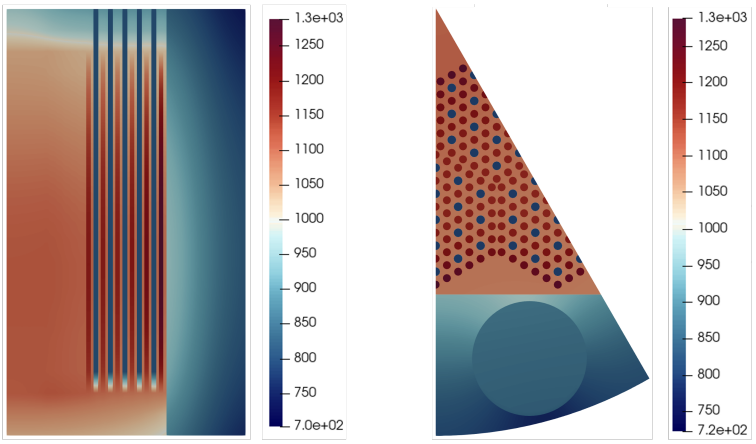

Figure 8: Temperature (K) distributions of the axial (left) and radial (right) mid-planes.

4.5 Multiphysics Depletion

A preliminary multiphysics microdepletion calculation was conducted for the rHPMR. This calculation comprised 51 depletion steps including the beginning of life (BOL). Each depletion step spanned a month except for the initial depletion step lasting 4 days which accounted for xenon buildup. For the depletion calculation, 5,424 depletion zones were defined (comprising 3 rings, 16 axial zones, and the number of pins in a $1/12^{\text{th}}$ core), with each zone associated with a dis-

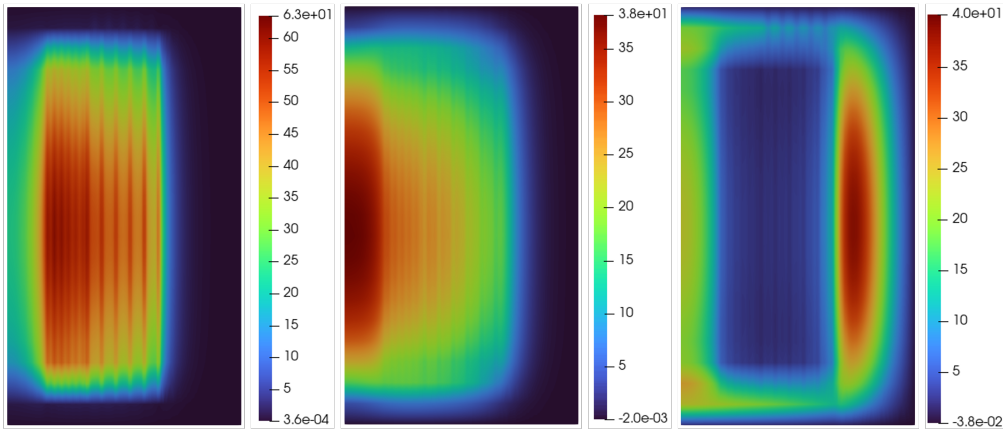

Figure 9: Unscaled fast (left), intermediate (middle), and thermal (right) flux distributions of the axial mid-plane.

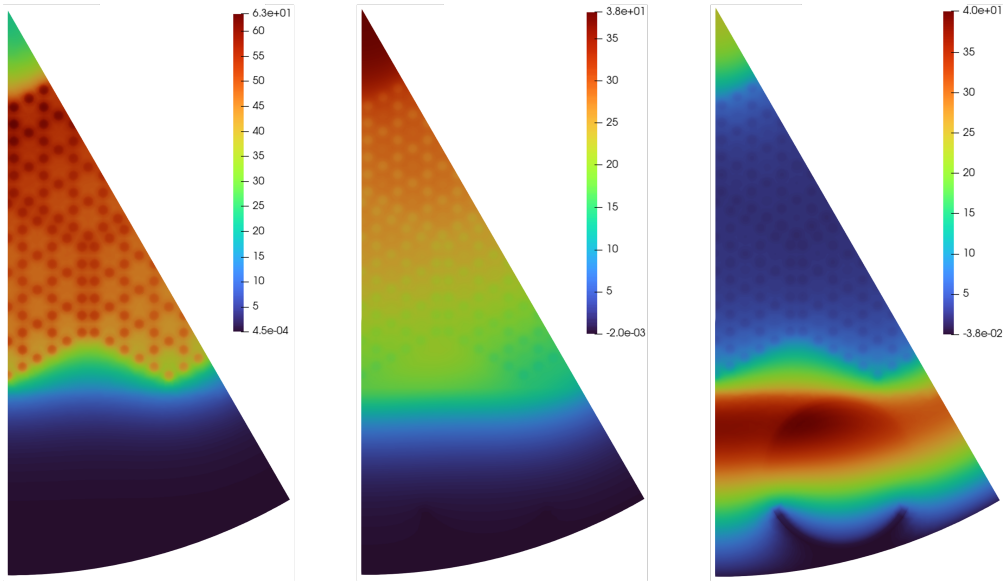

Figure 10: Unscaled fast (left), intermediate (middle), and thermal (right) flux distributions of the radial mid-plane.

tinct neutron scalar flux value. This level of detail for the depletion zoning was deemed essential for capturing the spatial variation of neutron flux within the reactor, given its thermal spectrum. Each of the 51 discrete ordinate eigenvalue calculations was performed during the depletion transient utilized 3 polar and 6 azimuthal angles in octant, consistent with the neutronics verification analysis outlined in Section 4.3. With these discretization conditions, the entire simulation process consumed 5.7 hours utilizing 240 processors on the INL Sawtooth cluster.

Fig. 15 illustrates the effective multiplication factors plotted against calendar days for the reactor's 4-year lifespan. The initial steep reactivity decline attributed to xenon buildup in the fuel can

be observed. The letdown curve of the effective multiplication factor indicates that, when considering thermal feedback in the calculation and homogenizing TRISO, the reactor goes subcritical after 1400 days. This outcome aligns with expectations, as the dispersion of fuel over a larger volume overestimates neutron absorption probability.

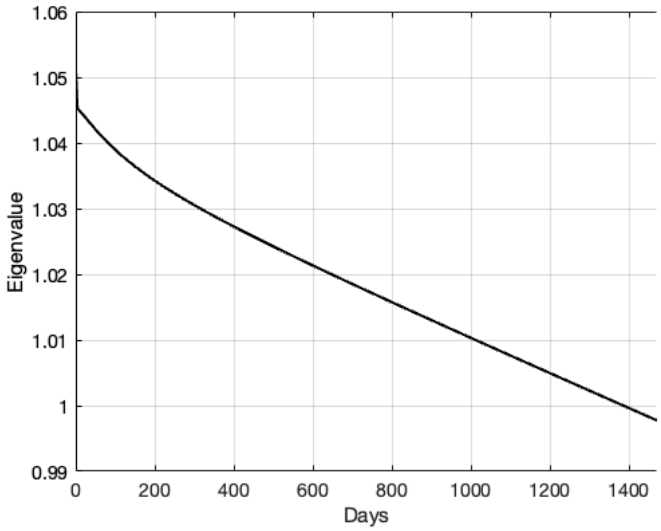

Figure 11: Change in k_{eff} vs. calendar days of operation of the rHPMR.

Fig. 12.a–b illustrates the power density distribution at both BOL and EOL for the axial midplane. The radial power distribution does not change meaningfully during the lifetime of the reactor. The only notable change is the amount of power deposited in the peripheral pins that is due to the beryllium reflector and the subsequent presence of thermal neutrons scattered back into the fuel. The radially-integrated power density distribution is shown in Fig. 12.c. The axial asymmetry of the power density distribution is clearly observed, which is due to the heat pipes penetrating in the top reflector that lead to higher neutron leakage in the upper part of the reactor.

The spatial distribution of selected nuclides was also computed at the EOL. The complete list of the tracked isotopes is reported in Appendix A together with their spatial distribution for each axial and radial layer. The spatial distribution of the nuclides is outputted from Griffin through a new postprocessor implemented for this work that enables user to obtain nuclide inventories with arbitrary spatial resolution without modifying the neutronic mesh. This allows the users to easily output inventory distributions compatible with the MELCOR or FATE requirements. In this work, 8 equally-spaced axial layers times two radial sectors, corresponding to the two assembly rings in

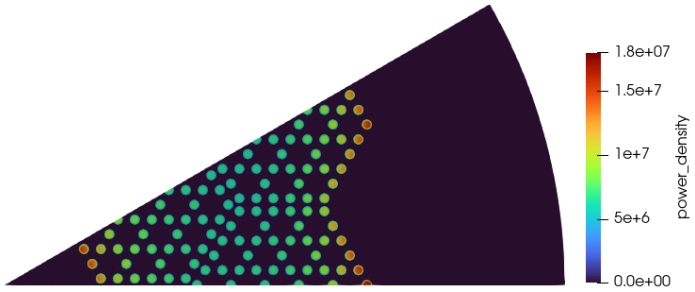

(a)

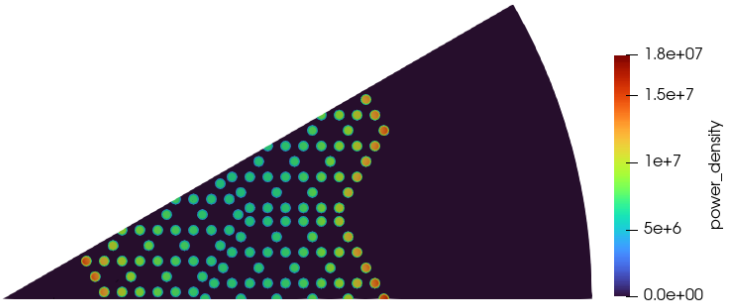

(b)

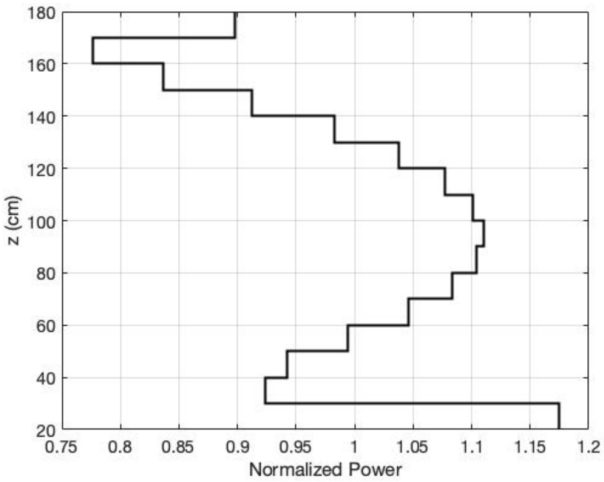

(c)

Figure 12: Power density distribution at (a) BOL and (b) EOL at the axial mid-plane, and (c) Radially-integrated normalized power distribution as a function of height for EOL.

the rHPMR, were chosen to output the inventory. No azimuthal dependence is tracked due to the fact that MELCOR is limited to solving RZ spatial distribution. For the sake of exemplifying the retrievable information from the simulation, the Pu-239, Xe-133, and Sr-90 number density spatial distribution for the two assembly rings as a function of the axial position is displayed in Figs. 13.a–c. It can be seen that the number density distribution for Xe-133 and Sr-90 closely follow the power

distribution due to the correlation with the fission reaction rate. In particular, the axial asymmetry of the nuclide inventory is noticeable, which reflects the asymmetry of axial power density profile. The Pu-239 number density distribution, on the other hand, exhibits a cosine spatial dependence with a much slighter axial asymmetry due to the influence of both fission of U-235 and absorption of U-238.

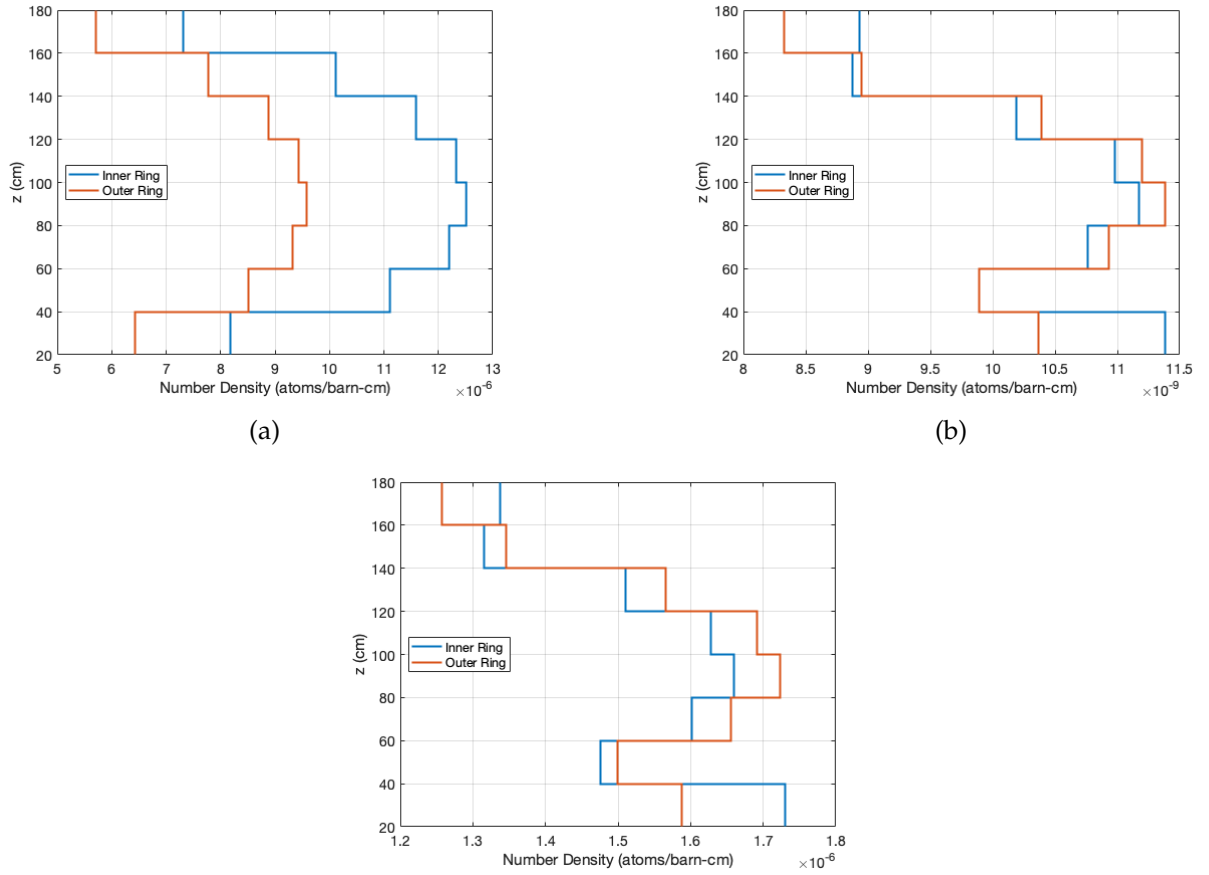

Figure 13: Ring-integrated number density of (a) Pu-239, (b) Xe-133, and (c) Sr-90 as a function of the axial position at EOL.

The time evolution of the nuclides during the reactor lifetime is shown in Fig. 14. It is noticeable that the three nuclides considered in the simulation evolve towards saturation, with Xe-133 reaching an equilibrium state after about 10 days that is comparable to the half-life of the nuclide. Pu-239 and Sr-90 follow a similar trend that is in line with larger values of the nuclides' half-life.

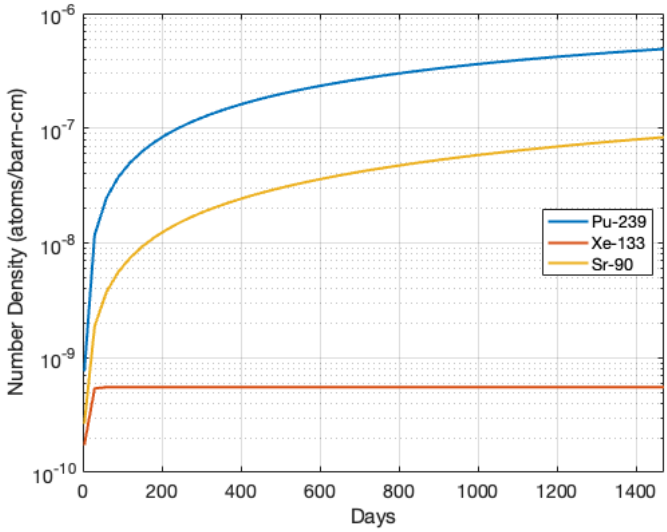

Figure 14: Pu-239, Xe-133, and Sr-90 total number density as a function of time.

4.6 Performance Optimization

Due to the computational expense of the depletion calculation, efforts were directed towards optimizing Griffin's performance through collaboration with the Nuclear Energy Advanced Modeling and Simulation (NEAMS) program. Through these optimizations, the execution time for a 4-year depletion calculation was reduced from 17.4 hours to 5.7 hours on 240 processors. This optimization effort addressed two performance bottlenecks in Griffin:

1. **Utilization of element-averaged cross sections:** Griffin offers an option to store element-averaged cross sections for use in the CMFD acceleration and residual evaluation. This option bypasses MOOSE kernels bound to material property evaluation and directly evaluates residuals using Griffin's sweeper, allowing users to control the frequency of cross section updates. With this option, cross sections can be updated only once at the start of neutronics solve at each Picard iteration, ensuring the incorporation of up-to-date temperature distributions or number densities and burnups from previous heat transfer or depletion solves.

2. **Elimination of unnecessary postprocessor and aux kernel evaluations:** Currently, Griffin computes flux scaling postprocessors and power density aux kernels at every linear iteration, resulting in a total of 6 material property evaluations per linear iteration. However, these postprocessors and aux kernels do not require evaluation at each linear iteration; in-

stead, they are only required after the neutronics solve at each Picard iteration. Therefore, a new capability was introduced to enable user-controlled execution, thereby eliminating unnecessary evaluations.

While the speedup achieved in this work is a factor of 3, it is expected to scale up with the number of variables used for cross sections' tabulation. Namely, if the burnup dependence is incorporated in the cross sections, the speedup will be more significant. Despite the optimization, negligible decreases in accuracy were observed, as depicted in Fig. 15, comparing the letdown curve of the original and optimized Griffin calculations. The optimized calculation exhibits an average difference of 2 pcm from the non-optimized result, primarily attributed to the dependence of cross sections on temperature at each quadrature point. The original calculation explicitly considers quadrature point-wise temperature-dependent cross sections in the residual evaluation, while the cross section averaging option utilized in the optimized calculation employs element-averaged cross sections. Nonetheless, these differences are inconsequential, as they are consistently less than 2 pcm across all depletion steps, and the use of the cross section averaging option is highly preferred for optimal performance.

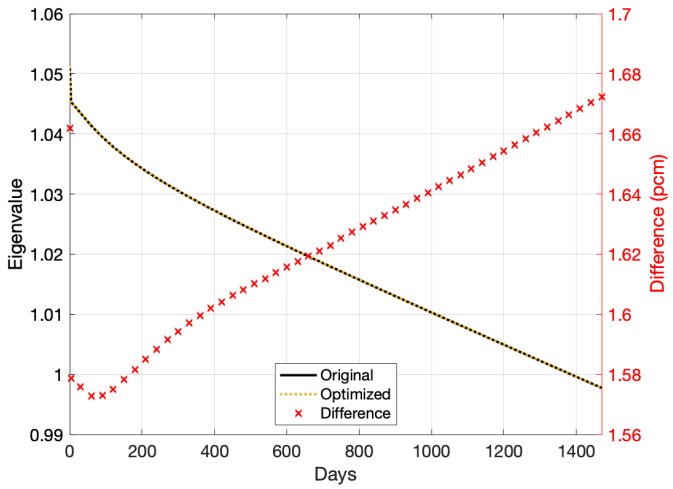

Figure 15: k_{eff} vs. calendar days of original and optimized Griffin depletion calculations.

5. Summary and Future Work

Ongoing research sponsored by MRP focuses on developing advanced modeling and simulation tools to enhance support for HPMR vendors and the NRC. During FY23, a significant achievement was made by demonstrating CRAB's capability of informing mechanistic source term calculations in MELCOR. In fiscal year 2024, current efforts have been directed towards the application of the OpenMC-CRAB workflow to investigate the rHPMR problem, which was formulated based on inputs from WEC to be representative of the eVinci^{TM} design.

This report highlights the progress made at INL to support this MRP-sponsored effort in FY24. Specifically, it provides the geometric and material specifications of the RHPMR, along with considerations of neutronic and thermal margins to validate the realism of the reactor. Additionally, it presents current results from the multiphysics microscopic depletion conducted using the OpenMC-CRAB workflow, including the effective multiplication factors over time, spatial power distribution, and spatio-temporal data on selected nuclides of interest. Furthermore, a summary of efforts to optimize the runtime of the multiphysics microdepletion workflow through collaboration with the NEAMS program is provided.

Future work will concentrate on enhancing the fidelity of the results and generating spatial transient results to inform MELCOR and FATE mechanistic source term calculations. To increase simulation fidelity, the following operations will be performed: (1) Explicit modeling of TRISO particles in the OpenMC reactor model for cross-section generation instead of relying on TRISO particles homogenized within the graphite compact. (2) Tabulation of microscopic cross-sections not only with respect to the local temperature but also the burnup to capture changes in the neutron spectrum due to compositional changes during the reactor lifetime. (3) Incorporation of a Sockeye-based heat pipes model to obtain time-dependent heat transfer coefficients for a more accurate description of heat transfer between the graphite monolith and heat pipes. A reactivity-initiated accident scenario will then be simulated to inform the mechanistic source term analysis performed with MELCOR and FATE.

REFERENCES

[1] P. A. Behne, M. K. Jaradat, N. Choi, S. Terlizzi, and V. M. Laboure, "Development of a bluecrab/melcor framework for supporting realistic mechanistic source term calculations in microreactors," Tech. Rep. INL/RPT-23-74793-Rev000, Idaho National Laboratory, 9 2023.

[2] J. D. Stempien, J. D. hunn, R. N. Morris, T. J. Gerczak, and P. A. Demkowicz, "Agr-2 triso fuel post-irradiation examination final report," Tech. Rep. INL/EXT-21-64279-Rev000, Idaho National Laboratory, 9 2021.

[3] N. Roskoff, V. Kucukboyaci, A. Levinsky, V. M. Laboure, J. R. Harter, A. X. Zabriskie, and L. C. Madeleine Charlot, "Modeling and analysis of a micro-reactor using the direwolf code suite," (Pittsburgh, PA, United States), International Conference on Physics of Reactors 2022 (PHYSOR 2022), 5 2022.

[4] J. Leppänen, "Serpent– a continuous-energy Monte Carlo reactor physics burnup calculation code.," tech. rep., VTT Technical Research Centre of Finland, 2015.

[5] E. R. J. Woodcock and T. C. Longworth, "Techniques used in the gem code for monte carlo neutronics calculations in reactors and other systems of complex geometry," *ANL-7050 Technical report*, 1965.

[6] M. Chadwick, P. Obložinský, M. Herman, N. Greene, R. McKnight, D. Smith, P. Young, R. MacFarlane, G. Hale, S. Frankle, A. Kahler, T. Kawano, R. Little, D. Madland, P. Moller, R. Mosteller, P. Page, P. Talou, H. Trellue, M. White, W. Wilson, R. Arcilla, C. Dunford, S. Mughabghab, B. Pritychenko, D. Rochman, A. Sonzogni, C. Lubitz, T. Trumbull, J. Weinman, D. Brown, D. Cullen, D. Heinrichs, D. McNabb, H. Derrien, M. Dunn, N. Larson, L. Leal, A. Carlson, R. Block, J. Briggs, E. Cheng, H. Huria, M. Zerkle, K. Kozier, A. Courcelle, V. Pronyaev, and S. van der Marck, "Endf/b-vii.0: Next generation evaluated nuclear data library for nuclear science and technology," *Nuclear Data Sheets*, vol. 107, no. 12, pp. 2931–3060, 2006. Evaluated Nuclear Data File ENDF/B-VII.0.

[7] P. K. Romano, N. E. Horelik, B. R. Herman, A. G. Nelson, B. Forget, and K. Smith, "Openmc: A state-of-the-art monte carlo code for research and development," *Annals of Nuclear Energy*,

vol. 82, pp. 90–97, 2015. Joint International Conference on Supercomputing in Nuclear Applications and Monte Carlo 2013, SNA + MC 2013. Pluri- and Trans-disciplinarity, Towards New Modeling and Numerical Simulation Paradigms.

[8] P. Nemec, A. Čaja, and M. Malcho, "Mathematical model for heat transfer limitations of heat pipe," *Mathematical and Computer Modelling*, vol. 57, no. 1, pp. 126–136, 2013.

[9] C. Matthews, V. Laboure, M. DeHart, J. Hansel, D. Andrs, Y. Wang, J. Ortensi, and R. C. Martineau, "Coupled multiphysics simulations of heat pipe microreactors using direwolf," *Nuclear Technology*, vol. 207, no. 7, pp. 1142–1162, 2021.

[10] J. E. Hansel, R. A. Berry, D. Andrs, M. S. Kunick, and R. C. Martineau, "Sockeye: A one-dimensional, two-phase, compressible flow heat pipe application," *Nuclear Technology*, vol. 207, no. 7, pp. 1096–1117, 2021.

[11] C. Lee, Y. S. Jung, H. Park, E. R. Shemon, J. Ortensi, Y. Wang, V. M. Laboure, and Z. M. Prince, "Griffin software development plan," Tech. Rep. INL/EXT-21-63185, Idaho National Laboratory, 6 2021.

[12] R.L. Williamson et al., "Multidimensional Multi-physics Simulation of Nuclear Fuel Behavior," *Jou. Nucl. Mat.*, vol. 423, no. 149–163, 2012.

[13] E. Shemon, Y. Miao, S. Kumar, K. Mo, Y. S. Jung, A. Oaks, S. Richards, G. Giudicelli, L. Harbour, and R. Stogner, "Moose reactor module: An open-source capability for meshing nuclear reactor geometries," *Nuclear Science and Engineering*, vol. 0, no. 0, pp. 1–25, 2023.

[14] S. Terlizzi and V. Labouré, "Asymptotic hydrogen redistribution analysis in yttrium-hydride-moderated heat-pipe-cooled microreactors using direwolf," *Annals of Nuclear Energy*, vol. 186, p. 109735, 2023.

[15] C.-S. Lin and W. S. Yang, "An assessment of the applicability of multigroup cross sections generated with monte carlo method for fast reactor analysis," *Nuclear Engineering and Technology*, vol. 52, no. 12, pp. 2733–2742, 2020.

Appendix A
Nuclides Spatial Distribution

Table 7: Distribution of fission product and actinide number densities at the EOL.

(a) Ag-111

	r	
z	8.596E-11	6.925E-11
	1.001E-10	8.657E-11
	1.256E-10	1.097E-10
	1.414E-10	1.235E-10
	1.455E-10	1.269E-10
	1.376E-10	1.196E-10
	1.192E-10	1.019E-10
	1.207E-10	9.476E-11

(b) Ce-144

	r	
z	3.723E-07	3.494E-07
	3.670E-07	3.738E-07
	4.205E-07	4.337E-07
	4.529E-07	4.680E-07
	4.609E-07	4.759E-07
	4.446E-07	4.574E-07
	4.097E-07	4.142E-07
	4.773E-07	4.376E-07

(c) Cs-134

	r	
z	7.136E-12	5.367E-12
	8.824E-12	7.224E-12
	1.152E-11	9.577E-12
	1.323E-11	1.104E-11
	1.369E-11	1.141E-11
	1.287E-11	1.066E-11
	1.089E-11	8.835E-12
	1.069E-11	7.855E-12

(d) Cs-137

	r	
z	1.493E-06	1.391E-06
	1.489E-06	1.504E-06
	1.722E-06	1.761E-06
	1.866E-06	1.911E-06
	1.903E-06	1.948E-06
	1.833E-06	1.869E-06
	1.680E-06	1.683E-06
	1.947E-06	1.767E-06

(e) I-131

	r	
z	6.048E-09	5.603E-09
	6.059E-09	6.061E-09
	6.992E-09	7.064E-09
	7.554E-09	7.637E-09
	7.689E-09	7.766E-09
	7.401E-09	7.451E-09
	6.776E-09	6.718E-09
	7.745E-09	7.005E-09

(f) Kr-85

	r	
z	5.042E-08	4.742E-08
	4.961E-08	5.074E-08
	5.690E-08	5.899E-08
	6.136E-08	6.377E-08
	6.249E-08	6.491E-08
	6.031E-08	6.239E-08
	5.560E-08	5.647E-08
	6.517E-08	5.984E-08

(g) La-140

	r	
z	2.600E-09	2.434E-09
	2.570E-09	2.605E-09
	2.941E-09	3.015E-09
	3.164E-09	3.247E-09
	3.217E-09	3.299E-09
	3.102E-09	3.170E-09
	2.857E-09	2.873E-09
	3.304E-09	3.024E-09

(h) Mo-99

	r	
z	4.266E-09	3.979E-09
	4.238E-09	4.274E-09
	4.864E-09	4.959E-09
	5.240E-09	5.347E-09
	5.329E-09	5.434E-09
	5.136E-09	5.219E-09
	4.720E-09	4.722E-09
	5.434E-09	4.953E-09

(i) Ru-103

	r	
z	3.409E-08	3.100E-08
	3.495E-08	3.421E-08
	4.092E-08	4.038E-08
	4.454E-08	4.395E-08
	4.543E-08	4.477E-08
	4.359E-08	4.283E-08
	3.953E-08	3.828E-08
	4.431E-08	3.926E-08

(j) Sb-125

	r	
	6.219E-09	5.634E-09
	6.408E-09	6.265E-09
	7.570E-09	7.467E-09
z	8.289E-09	8.178E-09
	8.476E-09	8.351E-09
	8.125E-09	7.978E-09
	7.336E-09	7.093E-09
	8.260E-09	7.271E-09

(k) Sr-90

	r	
	1.337E-06	1.257E-06
	1.316E-06	1.346E-06
	1.510E-06	1.565E-06
z	1.628E-06	1.692E-06
	1.659E-06	1.723E-06
	1.601E-06	1.656E-06
	1.476E-06	1.499E-06
	1.730E-06	1.588E-06

(l) Te-132

	r	
	3.551E-09	3.299E-09
	3.544E-09	3.558E-09
	4.080E-09	4.138E-09
z	4.403E-09	4.469E-09
	4.480E-09	4.543E-09
	4.314E-09	4.361E-09
	3.957E-09	3.938E-09
	4.536E-09	4.116E-09

(m) Xe-133

	r	
	8.933E-09	8.328E-09
	8.877E-09	8.949E-09
	1.019E-08	1.039E-08
z	1.098E-08	1.120E-08
	1.117E-08	1.138E-08
	1.076E-08	1.093E-08
	9.891E-09	9.889E-09
	1.138E-08	1.037E-08

(n) Pu-239

	r	
	7.311E-06	5.709E-06
	1.012E-05	7.769E-06
	1.159E-05	8.882E-06
z	1.232E-05	9.437E-06
	1.252E-05	9.577E-06
	1.219E-05	9.318E-06
	1.111E-05	8.503E-06
	8.176E-06	6.429E-06